Advanced Functional Materials

ADVANCED FUNCTIONAL MATERIALS
www.afm-journal.de

RESEARCH ARTICLE

Full-Spectrum White Emission from Boron Nitride Quantum Dots with Long-Term Stability Enabled by Selective Oxygen Tailoring

Yamei Ding[1] | Xianghong Niu[2] | Hengyang Xiang[4] | Xinming Zhuang[5] | Zaixing Yang[5] | Tao Xu[6] | Litao Sun[6] | Weiqiang Liu[7] | Xinran Wang[8] | Chunxiang Xu[6] | Haibo Zeng[4] | Jinlan Wang[3] | Li Tao[1]

[1]School of Materials Science and Engineering, Southeast University, Nanjing, China | [2]School of Science, Nanjing University of Posts and Telecommunications, Nanjing, China | [3]Key Laboratory of Quantum Materials and Devices of Ministry of Education, School of Physics, Southeast University, Nanjing, China | [4]College of Materials Science and Engineering, Nanjing University of Science & Technology, Nanjing, China | [5]School of Physics, Shandong University, Jinan, China | [6]SEU-FEI Nano-Pico Center, Southeast University, Nanjing, China | [7]Integrated Circuit Institute, Nanjing University of Aeronautics and Astronautics, Nanjing, China | [8]School of Integrated Circuits, Nanjing University, Nanjing, China

Correspondence: Haibo Zeng (zeng.haibo@njust.edu.cn) | Jinlan Wang (jlwang@seu.edu.cn) | Li Tao (tao@seu.edu.cn)

Received: 2 April 2026 | **Revised:** 26 April 2026 | **Accepted:** 5 May 2026

Keywords: full-specturm white emission | long-term stability | security authentication | selective deoxygenation | the third-generation nitride quantum dots

ABSTRACT

III-V semiconductor compounds, e.g. boron nitride and gallium nitride, are strategic candidates for next-generation miniaturized illumination with high-stability and integrated advantages, but face challenge in broad white emission in the visible region due to inherent bandgap limitation. Herein, this work reveals a trinity emitting strategy based on hexagonal boron nitride quantum dots (BNQDs) exhibiting full-spectrum white emission. This is featured with trichromatic fluorescent states, including dual energy migration channels from blue (2.9 eV) to green peak (2.5 eV) with charge delocalization effect, and red peak (2.1 eV) by induced dipole moment interaction. The resulting BNQDs exhibit an ultra-high color rendering index (CRI) of 95 and a wide-range adjustable correlated color temperature (CCT). Moreover, selective deoxygenation at the nitrogen atomic site of BNQDs purposefully decreases carrier loss and phonon scattering for a record quantum yield of 68.3% alongside exceptional thermostability to 573 K, and long-term optical stability whose performance decreased by only 4.7% when preserved in the air for 2.5 years. Our BNQD gives birth to ultra-stable white light emitting diodes, enabling codable optical signals for multi-level authentication with a low deviation ratio at $1/2\times10^{-22}$. This work provides an atomic-level regulation strategy of multiple luminescence states in single-component white-light materials for advanced optoelectronic applications.

1 | Introduction

Next-generation white-emitting lighting is evolving toward full-spectrum, ultra-stability, and environmental sustainability as the increased demand for healthy and intelligent displays [1–6]. Traditional mixed phosphors with UV or blue light-emitting diode (LED) chips suffer from self-absorption, stokes shift, and a complex process, causing low conversion efficiency [7]. All-inorganic lead halide perovskites with self-trapped exciton (STE) characteristics exhibit easy solution processibility for

Yamei Ding and Xianghong Niu contributed equally to this work.

[Correction added on May 25, 2026, after first online publication: The quality of the figures (1–6) has been updated in this version.]

efficient white-emitting properties, but are obstructed by the toxicity and instability issues [8–11]. Among diverse alternative candidates, the third-generation nitride semiconductors represent a promising avenue toward stable and miniaturized LEDs due to high thermal conductivity, electronic mobility, and integrated capability [12–15]. Nonetheless, current film growth and device techniques struggle to realize single-component broad white light emission based on wide-bandgap nitride.

Colloidal semiconductor quantum dots (QDs) are ideal nanomaterials to break through the bandgap astriction due to the quantum confinement effect and flexible regulatory advantages, making them highly promising for display and light sources [16–19]. Therefore, III-V compound based QDs have be well designed with full-color and thermostable lighting, but cannot afford single-component white emission [20–22]. Currently, edge doping and interface functionalization provide methods to realize single-component white emission for graphene and MXene QDs via constructing a charge-transfer transition. However, these strategies only generate two peaks (blue with yellow, or with red) in single-component QDs, insufficient to cover the entire visible light spectrum, with an ultralow value of color-rendering index (CRI) and a narrow range of carralted color temperature (CCT) adjustment [23–34]. Moreover, accompanying energy migration often brings about low quantum yield (QY), typically less than 40%, which restricts their applications. In response to the above challenges, nitride semiconductors demonstrate significant advantages—polarization effect helps separation of wave functions of electrons and holes to broaden white emission, and pure atomic surface environment without extra unpaired electron traps or unsaturated chemical bonds reduces carrier scattering to increase radiation recombination for enhanced QY and stability [35]. Hence, it is of tremendous significance if conceive a novel mechanism that allows high-efficiency full-visible-spectrum emission based on nitride QDs for the next-generation stable and healthy white lights.

In this work, we introduce a novel trinity emitting strategy based on hexagonal boron nitride (BN) QDs to independently construct dual energy migration channels from blue to green and red fluorescent states for single-component full-spectrum white emission. Furthermore, selective deoxygenation at the N site is implemented for enhanced QY of 68.3% and thermostability at 573 K to guarantee efficient and stable emission. On the basis of this, BNQD could yield a stable white LED (WLED) with a high CRI of 95 and a high-precision adjustable CCT. The device has been evaluated under different operating conditions with high reliability for more than 2.5 years, beneficial for a stable white light source and optical related safety certifications.

2 | Results and Discussion

2.1 | Design of Trichromatic States of BNQDs

BN precursor is well-selected without extra surface traps to construct multiple luminescent states for white emission through a hydrothermal treatment (Figure 1a). As a starting point, we select p-phenylenediamine (PPD) ligands with a primary amine and conjugated aromatic structure to manipulate charge delocalization from BN to ligands. Different PPD grafting sites are considered on the face or edge plane of BN. Both functionalization locations are feasible at thermodynamics based on the negative final free energy change. Such different configuration sites can coexist because the reaction Gibbs energy of initial (IS), transition (TS), and final (FS) states have no obvious change (Figure S1). We carried out molecular dynamics simulations using the Vienna Ab-initio Simulation Package (VASP), tracking the vibrations of the bandgap for different configuration sites (Figure 1b). The highest occupied molecular orbital (HOMO) has been affected obviously. Large carrier delocalization reveals a strong polarization effect with the help of the conjugated PPD ligands, and, consequently, produces bandgap variation. The green light peak takes shape. As a contrast, the HOMO and lowest unoccupied molecular orbital (LUMO) of urea passivated BNQDs is steady, thus in the blue region (Figures S2 and S3).

For another necessary red-light state, NMP is chosen to offer a polar solvation effect for enhanced coupling interaction around amine functional groups at the edge [36]. After the absorption of light (10^{-15} s) with excess vibrational energy via Frank–Condon transition, vibrational relaxation and solvent relaxation takes place to the band edge (10^{-12} s) [37]. When solvation dynamics slows down to the time scale of fluorescence decay (10^{-10}–10^{-9} s), a set of ensemble sub-levels will emerge for broadening spectrum. Our first-principles calculations reveal that the bandgap diminishes gradually with an increase in the number of solvation molecules. This phenomenon can be attributed to the enhanced induced dipole moment interaction, as corroborated by the Lippert–Mataga equation (Figure 1c, Figure S4). In contrast, the bandgap of QDs in ethanol solvents barely changes (Figure S5), consistent with our previous work [22]. Therefore, involved solvation distribution, together with different functional configuration sites bring about new green and red fluorescent states and leads to multiple ensemble sub-levels with red-shifting broadening from the highest emitting energy level (blue emission) to the special band edge (red emission) for white emission.

Based on the above design, our-prepared QDs are engineered with independent trichromatic peaks (Figure 2a). A blue peak (2.9 eV) occurs due to quantum confinement as BN nanosheets are tailored into QDs. Two new luminescent peaks are emerged due to synergetic effects of functional configuration (2.5 eV) and solvation distribution (2.1 eV). Then, temperature-dependent photoluminescence (PL) spectra of both urea and PPD passivated QDs are conducted with increasing temperature from 100 to 300 K (Figure 2b). Full-width at half-maximum (FWHM) of the broadband emission peak *vs* temperature was plotted to obtain the Huang–Rhys factor (S) related to the electron–phonon coupling strength according to Equation 1:

$$\mathrm{FWHM} = 2.36\sqrt{S}\hbar\omega_{phonon}\sqrt{\coth\frac{\hbar\omega_{\mathrm{phonon}}}{2\mathrm{K_B T}}} \quad (1)$$

here, S is the Huang–Rhys factor, $\hbar\omega_{\mathrm{phonon}}$ is the phonon frequency, and $\mathrm{K_B}$ is the Boltzmann constant [38]. We got an S value of 0.92 for the urea passivated QDs, while 24.69 for the PPD passivated QDs, which proving the broadening of the wide band emission covering the visible light region.

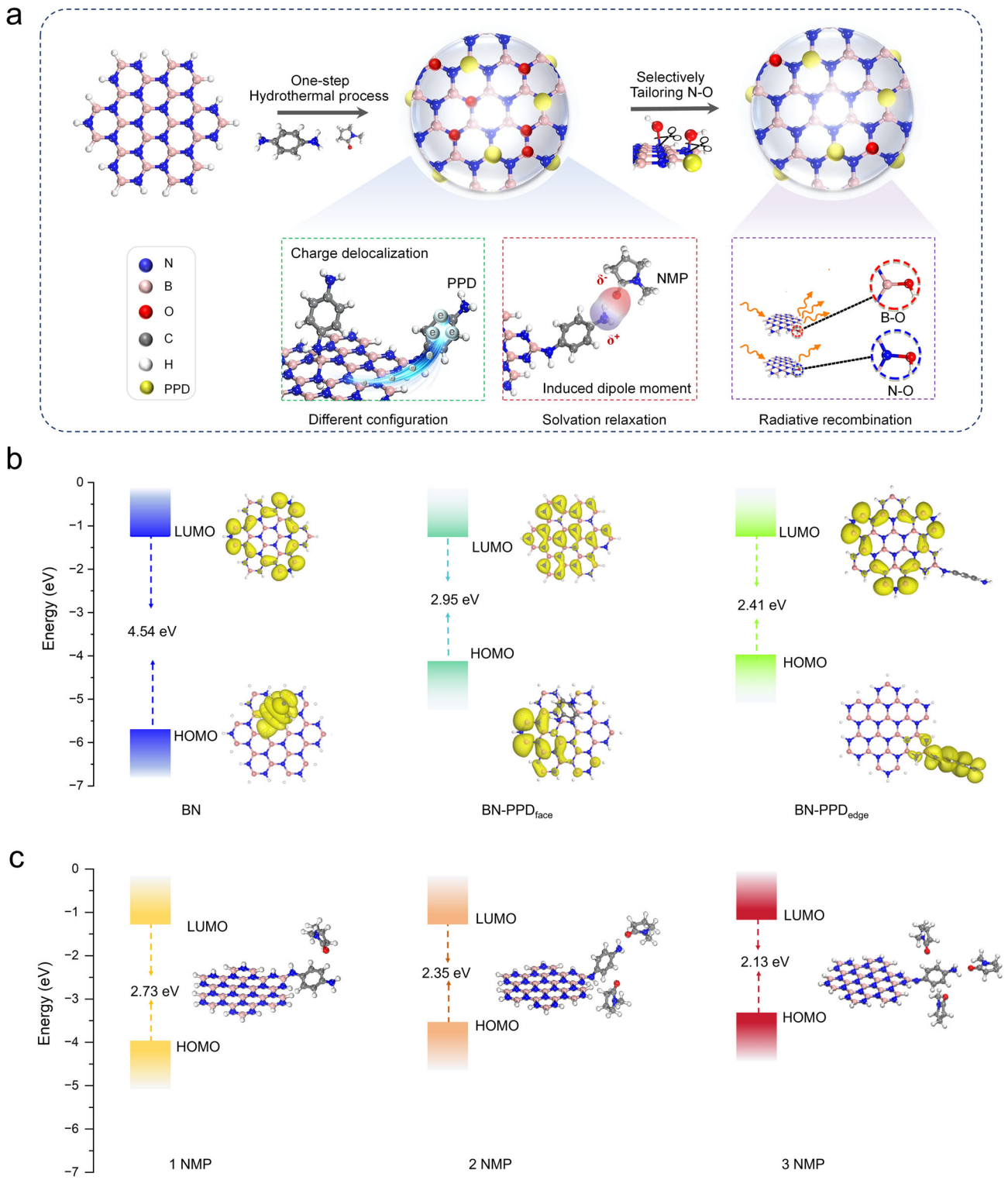

FIGURE 1 | (a) Schematic illustration of the synthetic strategy of white BNQDs. (b) HOMO-LUMO plots of BN functionalized by PPD on the face or edge plane. (c) HOMO-LUMO plots of BN functionalized by PPD surrounding different quantities of NMP molecules.

As the excitation wavelength red-shifts, the spectrum varies from excitation-dependent to excitation-independent properties (Figure 2c). This feature has neither been seen in precursors, manifesting that new luminescence peaks arise from the structural interaction of BN and PPD, and perform independently (Figure S6). UV absorption with two characteristic peaks at 325 and 485 nm, implies two types of excited energy absorption in the high-energy and low-energy regions (Figure S7) [39]. The fluorescence decay curve can be fitted by a two-exponential localized lifetime, corresponding to two carrier radiation recombination channels, as well (Figure 2d) [40].

Based on the above demonstration, we propose a universal mechanism as a figure of merit for rationally broadening spectrum.

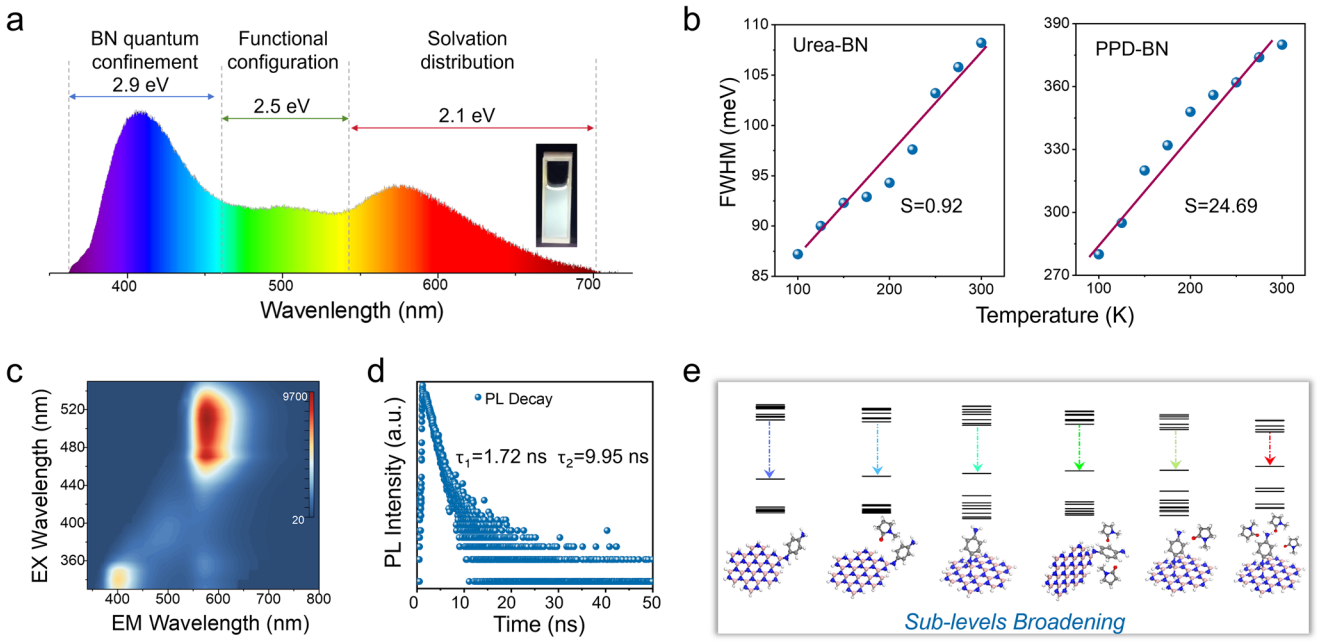

FIGURE 2 | (a) Photoluminescence spectra with optical image of BNQDs under 365 nm irradiation. (b) FWHMs of the urea and PPD passivated BNQDs at 365 nm as a function of temperature. (c) 2D pseudocolor map of excitation-emission spectra of BNQDs. (d) Time-resolved PL decay curves of BNQDs at 380 nm. (e) Illustration of the formation of widened sub-levels.

In this work, PPD functionalized configurations facilitate the charge delocalization effect, while polar solvent distributions around cause electron-phonon coupling. They established dual energy transfer channels and combined synergistically for the broadened sub-levels among trichromatic states (Figure 2e). Therefore, reported white QDs whose strategies related to edge functionalization, co-doping, and electronic coupling all aim at the formation of an energy transfer channel with expanded sub-levels to the low energy region (Table S1) [23–32]. In this principle, sub-levels are dynamic in which prominent factors compete and cooperative with each other such as large distortions, oxygen traps, and relaxation sites [37]. Macroscopic optical property is decided by the dominant energy state domains. For further proof, we re-prepared a new single-component white carbon dot by citric acid doping with 1, 5-diaminaphthalen based on this mechanism, where the sub-levels are dominated by relaxation of n-π charge transfer between abundant oxygen functional groups and aromatic ligand (Figures S8 and S9, Table S2).

2.2 | Selective Oxygen Tailoring

Figure 3a shows good homogeneity and dispersion of as-prepared BNQDs with an average size of 3 nm after the PPD passivation (Figure 3b, Figure S10). It also provides steric hinderance to suppress long distance order of layered BN nanoplate (Figure S11) and reduce radiation quenching, leading to discrete and pure QD with single (002) facets, as confirmed by grazing incidence X-ray diffraction (GIXRD, Figure 3c) [41]. However, the QY is only 13.98%, lower than expected. Observed from the Fourier transform infrared spectroscopy (FTIR), a large number of oxygen-containing functional groups have been formed with stretching vibration bands of N—O (1500 cm^{-1}) and B—O (1270 cm^{-1}), affecting efficient carrier radiation (Figure S12) [39]. The first-principles calculations demonstrate the effect of different oxygen sites on carrier dynamics. The band gaps of QDs are less affected by the B—O groups since the energy levels of B—O bonds are far from the frontier orbitals of QDs (Figure 3d). Another part of B—O as a fixed component linking the PPD and BN skeleton junction on the face and on the edge is also considered, which has less effect on the energy level structure of QDs as well (Figure S13). That is, the B—O bonds that can be reduced or inserted at contrast, while the energy level of N—O bonds is located around the band edges, which could effectively affect the photogenerated carrier dynamics (Figure 3e). Specifically, combined with the nonadiabatic molecular dynamics simulations (NAMD), the surfaced N—O impurity (Figure 3f, Figure S14), which does not directly trap carriers due to a relatively low energy orbital compared with PPD, its strongly vibrating electronic state will significantly enhance the electronic phonon coupling to the HOMO. For the edged N—O impurity, as excited electron re-turning to the ground state, B—O bonds allow carriers to go through smoothly, whereas N—O bonds can rapidly capture the carriers to hinder radiative recombination (Figure 3g, Figure S14). Therefore, removal of N—O bond is necessary to reduce electronic phonon coupling for optimization of optical performance and stability.

We proposed a selective deoxygenation strategy utilizing the activity difference of B and N sites. As a result, the content of the oxygen element decreases from 13.9% to 5.4% (Table S3). These changes are observed in FTIR with weakened bonds of N—O and B—O (Figure S12a) [39]. In X-ray photoelectron spectroscopy (XPS), the signals of B elements can be divided into B—N (190.4 eV) and B—O (191.4 eV) (Figure S12b,c). Peaks at 398.0 and 399.9 eV in the high-resolution spectra of N1s should be assigned to N—B and N—O, respectively (Figure 3 h) [42]. In comparison to B—O, N—O bond has been preferentially eliminated by hydrazine

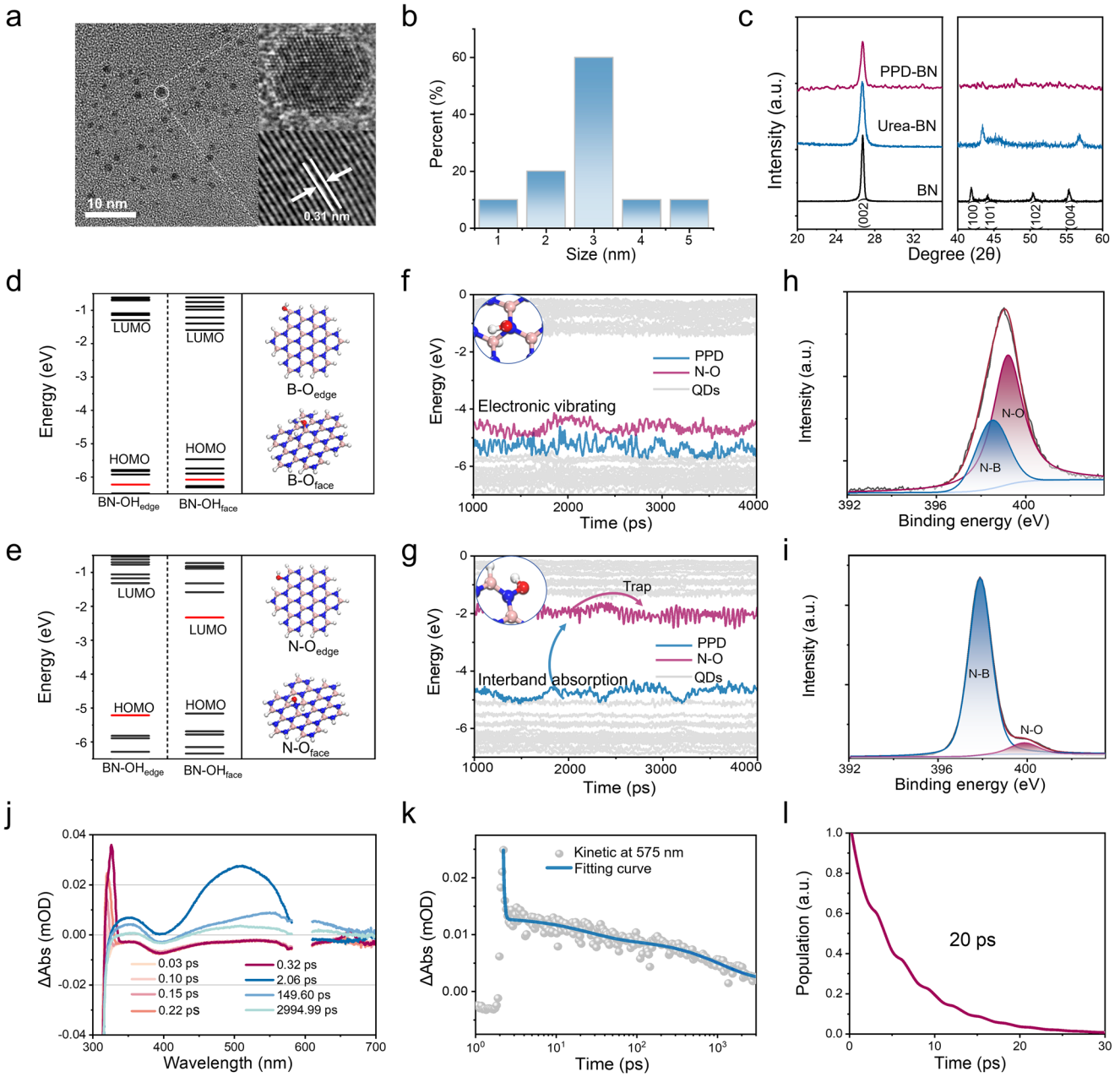

FIGURE 3 | HRTEM images (a) and size distribution (b) of BNQDs. (c) GIXRD patterns of pristine BNQDs, PPD-BNQDs, and urea-BNQDs. Variation of bandgap and energy levels of BNQDs with B—O (d) and N—O (e) bonds on the face and edge sites. Time evolution of frontier orbital energies of BNQDs with N—O bond on the face (f) and edge (g) obtained from NAMD calculations. The blue and red energy state trajectory are mainly contributed by the PPD functional group and impurity oxygen groups, respectively. The high resolution N1s XPS spectra of BNQDs before (h) and after (i) deoxygenation. (j) Femtosecond transient absorption spectra at indicated delay times from 0.03 ps to 3 ns at 300 nm irradiation. (k) Kinetic decay traces with a fitting curve in blue. (l) Averaged photogenerated carrier trapping dynamics of BNQDs with the N—O bond at edge sites.

hydrate after deoxygenation with a greater reduction of peak area due to the higher activity of at the N site (Figure 3i). This process has no effect on size distribution and polarization of BNQD (Figures S15 and S16).

Then, we systematically investigate the influence of selective deoxygenation on the optical properties of QDs using fs transient absorption (fs-TA) measurements (Figure S17). TA spectra at different specific delay time are depicted with a strong ground-state bleaching (GSB) signal centered at 320 nm behind closely the 300 nm laser, which matches with the peaks in the steady state absorption of QDs and indicates state filling transition (Figure 3j) [43, 44]. This bleach disappears at around 0.32 ps, which is longer than that of control BNQDs (0.15 ps), implying rapid charge transfer from the excited state to the emissive state. We attribute this bleaching difference to more population of charge carrier in the particular quantized state or a larger separation energy guarantees the high-level exciton states that lead to piling up of more excitons [45]. A broad negative peak centered at about 410 nm rises in the range of steady PL spectrum, corresponding to stimulated emission (SE). Two samples exhibit the same position of SE with maintained excited-state behaviors, which

is proved by PL (Figure S18). A major difference is the strength of stimulated emission, which has been proved to increase QY [43]. A positive signal at 500 nm is ascribed to the excited-state absorption (ESA) [46, 47]. The change of Abs in the time domain at 575 nm is revealed for the detailed relaxation channels of the excited carriers of QDs (Figure 3k). Three distinctive decay components were derived and fitted lifetimes of 80 fs, 25.2 ps, and 1.34 ns, respectively. The excited carriers have excess energy after excitation, and experience Coulomb-induced thermalization within the first few tens of fs [44]. One part of the carriers will experience a nonradiative transition to the ground state within 25.2 ps, which is consistent with our calculation at around 20 ps (Figure 3j). The others at surface and edge states emit mixed broad band fluorescence by the recombination of electrons and holes within 1.34 ns, indicating that excitons possess stable radiative recombination channels. Therefore, deoxygenation ensures the efficiency of radiation recombination in theory and experiments (Figure S19) [48].

2.3 | Boosted Efficiency and Long-Term Stability

Therefore, the QY had improved from 13.98% to 68.3%, with longer fluorescent lifetime, outperforming than other single-component WQDs (Figure 4a, Figure S20). Moreover, a stable BN skeleton and selective oxygen tailoring endow QDs with exceptionally long-term optical stability. The performance decreases by only 4.7% when stored in the air for 2.5 years, and maintains 89.5% of the initial efficiency under continuous heating at 200°C (Figure 4b,c). As an important parameter for evaluating chromatic shift in white light, CCT of BNQDs maintained a low deviation rate of 0.8% upon heating, significantly lower than that of control samples of 3.0% (Figure 4d). Under continuous heating at 200°C, the deviation rate rises to just 3.1%, also far below the control sample of 12.6% (Figure 4e). Moreover, burning tests (flame temperature at least 280°C) verify that the QD film has flame retardancy due to the inheritance of gas-barrier property from BN (Figure S21). Taking together with a radar map, target BNQDs perform higher thermal conductivity, more stable optical performance, and lower deviation rate after deoxygenation (Figure 4f). To evaluate the application potential of BNQDs in full-visible-spectrum solid-state lighting, a WLED has been fabricated by integrating QD-based optical films into a 365 nm LED chip (Figure 4g). The WLED exhibits broadened trichromatic fluorescent peaks with an FWHM of 300 nm in the solid state, wider than other single-component white light due to the π–π stacking between QDs and the further redshift of the red-emitting peak during solidification (Figure 4h). A high CRI of 95 and CIE coordinates of (0.33, 0.32) is realized, which could perfectly restore the color of objects (Figure 4i). With the help of selective deoxygenation, the LED device shows better heat dissipation with lower surface temperature from infrared thermal images (Figure 4j, explained in Supporting Information). The trichromatic fluorescence peaks and corresponding CCT remain stable at high temperatures of 573 K and voltages of 12 V, without noticeable change in positions (Figure 4k, Figure S22a). The luminance and CIE coordinates of the deivce is steady under continuous ultraviolet light irradiation (Figure S22b). Furthermore, the luminance decreases by only 7.2% in an air condition with 80% humidity due to the coordination of hydrophobic PDMS and steric hinderance of QD ligands (Figure S22c,d). Following comprehensive stability assessments, BNQDs demonstrate exceptional stability, rendering them highly suitable for long-term lighting and other optical related sustainable energy applications [49, 50].

2.4 | Multiple-Level Authentication

Benefiting from independently regulated trichromatic fluorescent peaks, CCT modulates from warm white (4580 K) to cold white (11045 K) via controlling the precursor ratios to meet different demand for color critical high-level lighting scenes (Figure S23, Table S4). During which, the values can be precisely regulated with high accuracy to the tens. Therefore, BNQD offers superior tuning flexibility and stability for safety authentication related to light communication, compared to monochromatic QDs that relying solely on the intensity changes of the fluorescence. Figure 5a illustrates the working principle of the single-challenge, multichannel-response security authentication based on BNQDs. First, an optical matrix with "4 by 4" units has been prepared from BNQD arrays with different trichromatic ratios. It emits positive white emission via regulating the CCT within the range from 5000 to 7000 K, 10^{32} permutations with large data volumes can be obtained, larger than the encoding capacity ($\sim 10^{20}$) of rudimentary physical unclonable functions (PUFs), manifesting compelling resistance to counterfeiting attempts (Figure S24). On the base of this, three optical signals including CCT (R_1), fluorescence intensity (R_2), and relative peak intensity (R_3) are subsequently in situ recorded and represented as the responses. A digitalization process is then performed, which compares with pre-established threshold values to generate binary output values of "0" or "1" logic states. In order to enhance the data verification levels of user authentication, four channels (C_1-C_4) are built through pairwise and overall combination of binary responses (R_1-R_3). These multichannel-responses can be converted to combinatorial password via five logic functions ("OR", "AND", "XOR", "NOR" and "XNOR"). Taking Channel 4 as an example, a password with combined letters and numbers is architected via a binary threshold treatment of three paratactic inputs (Input-1, Input-2, and Input-3), followed by five distinct logical functions (Figure 5b). The password is dynamically adjusted by the threshold algorithm set and the random logic protocol. The output values of "1" and "0" correspond to the "on" and "off" states, shown in purple or gray. Meanwhile, four channels can be employed and combined into a binary barcode or quick-response (QR) code by introducing a binary converter (Figure 5c,d). In contrast to a conventional PUF that could only generate a single key, dynamic passwords and four keys are generated in a single optical matrix, enabling multiple-level authentications. Users can also freely combine their own authentication keys for their specific requirements, facilitating robust security through multifactor authentication.

Comprehensive application demonstrations of this design is shown in Figure 6. A stable and bright white-emitting source based on BNQD matrix has been used for display, first. Three optical singals have been extracted and converted as digitized responses in four channnels. During authentication, users enter the password to obtain the independent keys. This match proceeded to the 4th layers, each operating with an independent

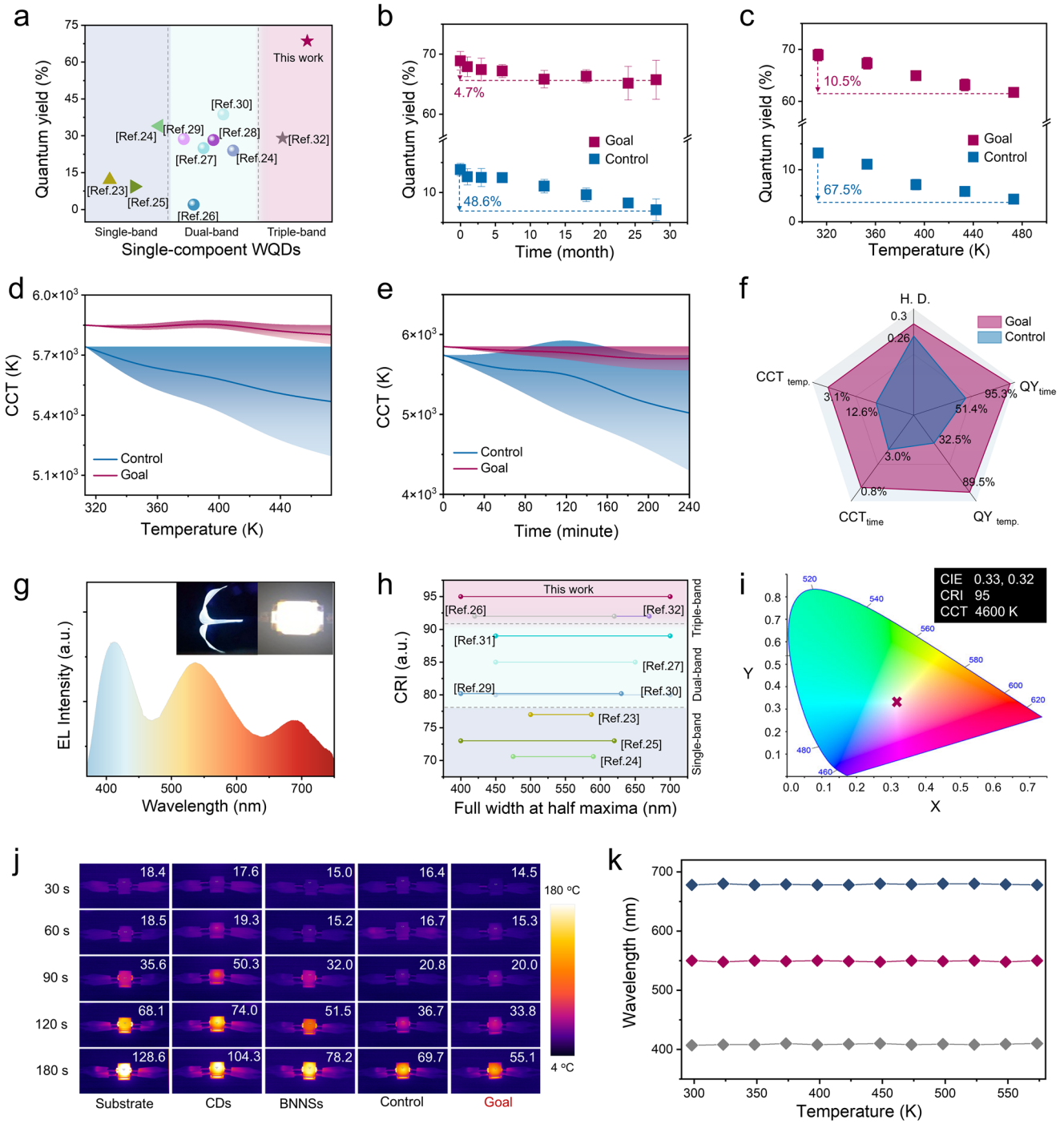

FIGURE 4 | (a) The QY comparison of reported single-component WQDs. QY changes of control and goal BNQDs under different times (b) and temperatures (c). (d) CCT deviation of control and goal BNQDs under different temperatures. (e) At 200°C, CCT deviation of control and goal BNQDs under different times. (f) The radar map of performance comparison based on liquid-phase heat dissipation (H. D.), QY decline rate, and CCT deviation ratio under different times and temperatures, respectively. (g) Electroluminescence spectrum of WLED based on BNQD films. (h) The comparison of FWHM and CRI of the reported single-component white emission. (i) CIE coordinates of WLEDs. (j) Thermal imagery diagrams of different QD-based LEDs under 9 V as a function of time. (k) The positions of WLED fluorescence peaks as a function of working temperature.

"key and feature" mechanism. Only when all four layers were successfully matched successfully with the binary code stored in the data server, the system return a "Pass", completing the anti-counterfeiting verification. Taking all permutation combinations into consideration, we assess the accuracy and security level via calculating deviation rate of CCT signals under $1/2\times10^{-22}$ with high-fidelity at elevated temperature according to Equation 2:

$$P(m,n) = \sum_{i=0}^{n} B(i,n)\,P(m/i) \tag{2}$$

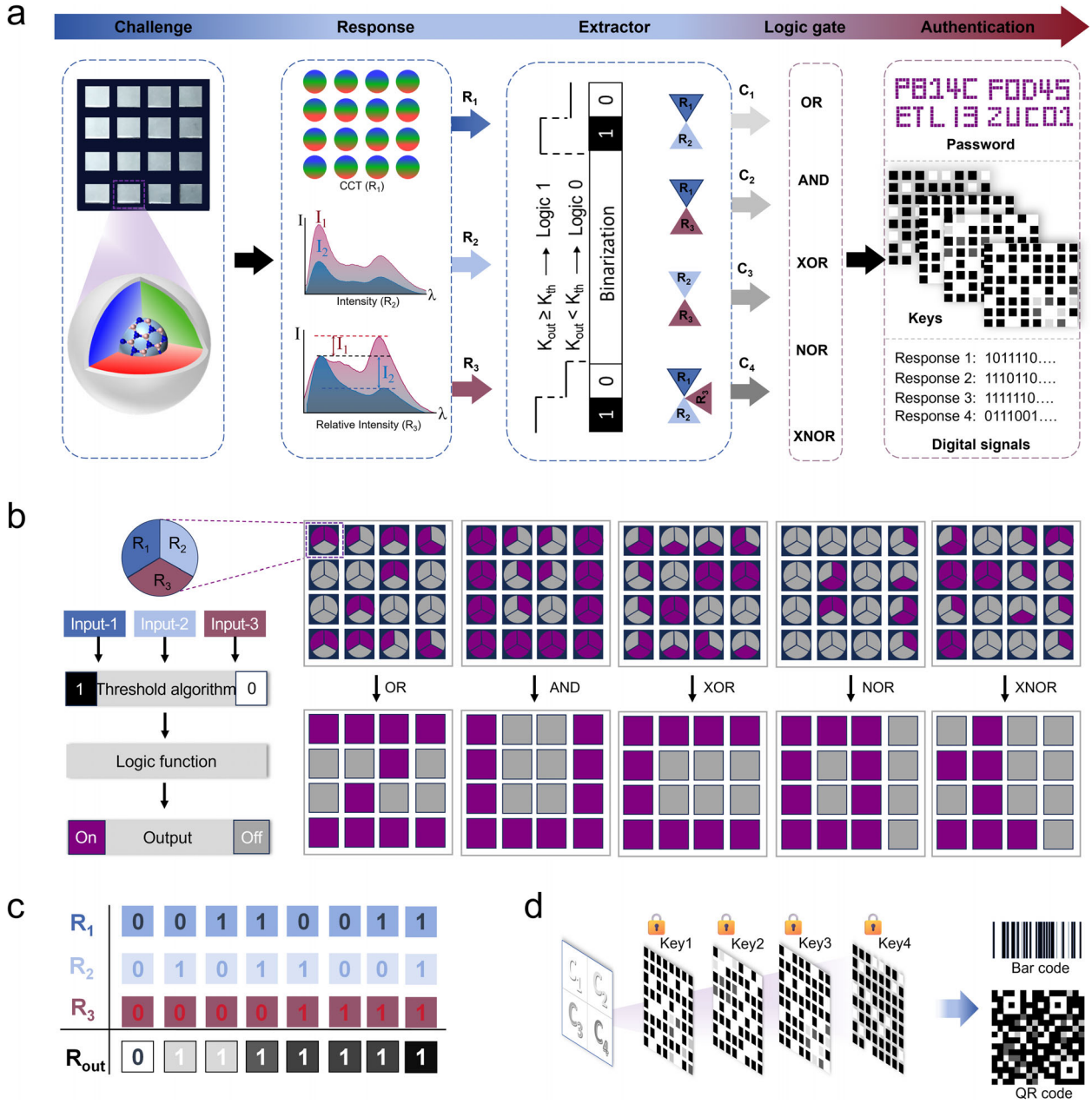

FIGURE 5 | (a) Single-challenge and multichannel-response authentication process based on BNQDs with three optical parameters. (b) Decryption demonstration of three responses using five logic functions for password generation in Channel 4. (c) Binary signal generation rules of three responses in Channel 4. (d) Schematic images of four authentication keys combined from four channels based on a single optical matrix for bar codes and QR codes.

where,

$$P(m/i) = C_i^m P_{error}^m (1 - P_{error})^{i-m} \quad (3)$$

P (m, n) is the conditional probability of *m* errors in bits transmitted in the *B* states, *B (i, n)* is the *i* bits transferred in the bad state of the channel from *n* frame, P_{error} is the probability of errors in the *B* state, and C_i^m is the number of *i* combinations of from *m* [51].

If user identification fails due to password theft or forgotten, and encoding error during signal conversion, logic protocols and user passwords stored in the code library can be redefined and upgraded accordingly. Meanwhile, matrix units based on QDs are easy to be realigned with new permutations or substitutes to offset encoding errors of incorrect units. Then, the final data server was updated accordingly due to these adjustments or as per the user's specified requirements. Thereby, in contrast to traditional transistor-based logic gates with intricate manufacturing processes and multiple components to switching a logic signal [52], this authentication system model generates large data centers, multi-level security authentication channels, and reliable signal correction in single-component BNQDs, offering a powerful and practical solution for protecting important information protection and authenticity verification.

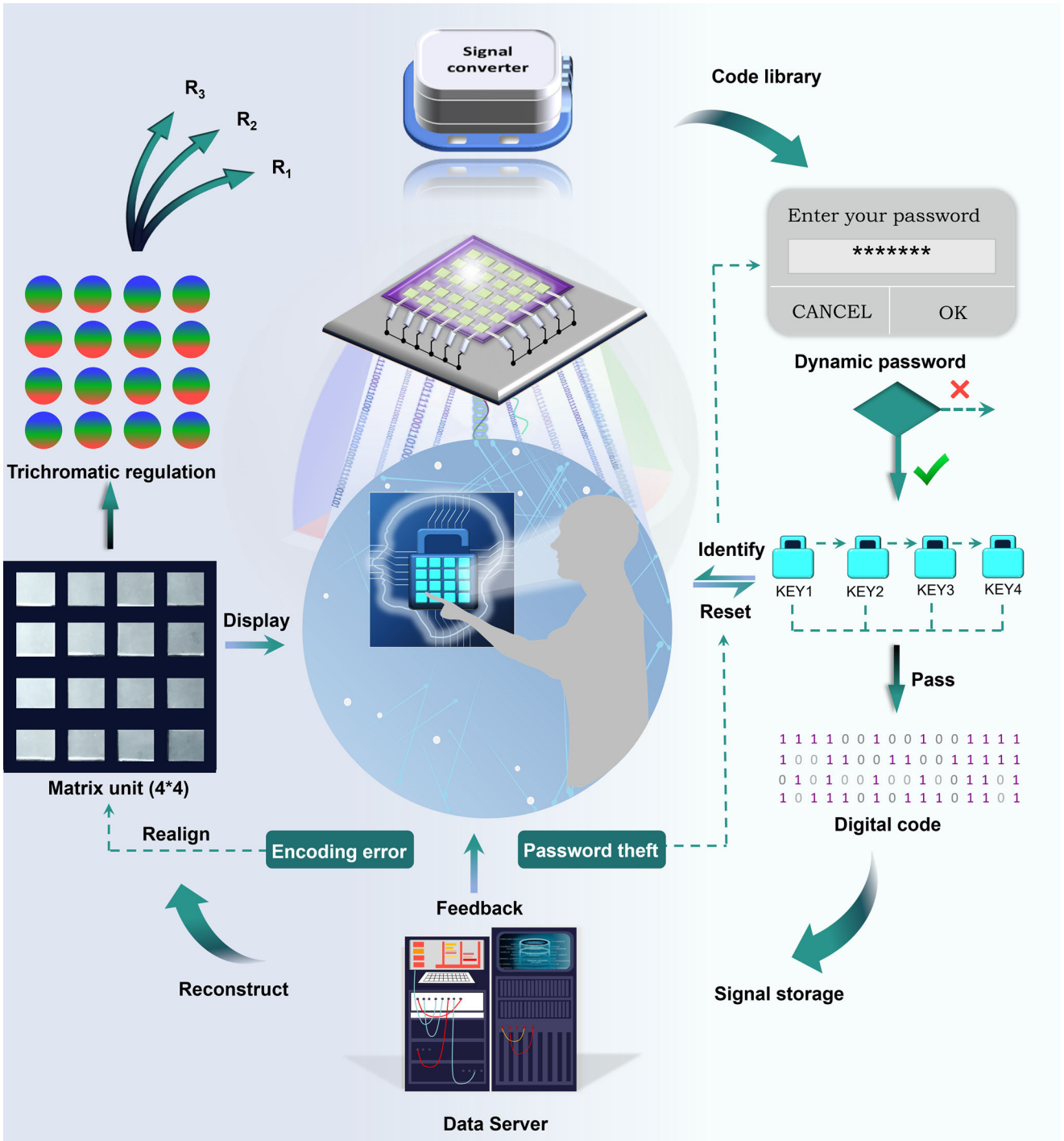

FIGURE 6 | Multi-level authentication demonstration enabled by BNQD based optical matrix. Three responses are extracted and converted into dynamic passwords, four channel keys, and digital signals. Users get keys via entering the correct passwords for multi-level authentication and acquire feedback from the data server.

3 | Conclusion

This work unseals a novel and universal design strategy to showcase single-component BNQDs that yield full-spectrum white emission with a high CRI of 95 and tunable CCT from 4580 to 11045 K. The broadband white emission comes from trichromatic peaks linked by transferred sub-levels via cooperative functionalized configuration and solvation distribution. Selective deoxygenation at N atomic site of BNQDs is designed for a record QY (68.3%), thermostability (300°C), and optical stability over 2.5-year. This enables the reliable WLED for multi-level security authentication with high-precision at a low deviation rate ($1/2\times10^{-22}$). This work presents a promising strategy to regulate single-component white nanomaterials, while inspiring further research on smart quantum structures for intelligent illumination and light communication.

Acknowledgements

We thank the National Supercomputing Center of Tianjin and Big Data Center of Southeast University for the use of computational resources. This work was supported by the National Natural Science Foundation of China (T2321002,22033002, 52131304, and 92164102), the National Key R&D Program of China (2022YFB4400100), the Jiangsu Province Key R&D Program (BE2023009-3) and Basic Research Program of Jiangsu Province (BK20222007).

Conflicts of Interest

None of the authors have a conflict of interest to disclose.

Data Availability Statement

The data that support the findings of this study are available from the corresponding author upon reasonable request.

References

1. Y. W. Chen, J. Wang, X. B. Xu, et al., "Efficient and Bright White Light-Emitting Diodes Based on Single-Layer Heterophase Halide Perovskites," *Nature Photonics* 15 (2021): 238–244, https://doi.org/10.1038/s41566-020-00743-1.

2. M. Zhao, Z. Y. Yang, L. X. Ning, and Z. G. Xia, "Tailoring of White Luminescence in a $NaLi_3SiO_4:Eu^{2+}$ Phosphor Containing Broad-Band Defect-Induced Charge Transfer Emission," *Advanced Materials* 33 (2021): 2101428, https://doi.org/10.1002/adma.202101428.

3. D. I. Son, B. W. Kwon, D. H. Park, et al., "Emissive ZnO-Graphene Quantum dots for White-Light-Emitting Diodes," *Nature Nanotechnology* 7 (2012): 465–471, https://doi.org/10.1038/nnano.2012.71.

4. S. Reineke, F. Lindner, G. Schwartz, et al., "White Organic Light-Emitting Diodes with Fluorescent Tube Efficiency," *Nature* 459 (2009): 234–238, https://doi.org/10.1038/nature08003.

5. S. Y. Qiao, X. D. Wu, J. J. Dong, et al., "Sterically Hindered Heterometallic Polyhedral Pairs in Halide Perovskite Derivative Enable Energy-Transfer-Enhanced Singlet Self-Trapped Excitons for Full-Spectrum White Light Emission," *Advanced Functional Materials* 36 (2025): 25709, https://doi.org/10.1002/adfm.202525709.

6. E. P. Yao, Z. L. Yang, and L. Meng, "High-Brightness Blue and White LEDs Based on Inorganic Perovskite Nanocrystals and Their Composites," *Advanced Materials* 29 (2017): 1606859, https://doi.org/10.1002/adma.201606859.

7. J. W. Chen, K. Y. Ji, L. J. Dai, et al., "Nanoscale Heterophase Regulation Enables Sunlight-Like Full-Spectrum White Electroluminescence," *Nature Communications* 16 (2025): 3621, https://doi.org/10.1038/s41467-025-58743-0.

8. S. Wang, C. Wang, Y. K. Wang, et al., "Local Lattice Softening in Semiconductor Quantum Dots for Efficient White Light-Emitting Diodes," *Nature Photonics* 19 (2025): 952–959, https://doi.org/10.1038/s41566-025-01716-y.

9. S. Kahmann, E. K. Tekelenburg, H. Duim, M. E. Kamminga, and M. A. Loi, "Extrinsic Nature of the Broad Photoluminescence in Lead Iodide-Based Ruddlesden-Popper Perovskites," *Nature Communications* 11 (2020): 1–8, https://doi.org/10.1038/s41467-020-15970-x.

10. J. Yin, R. Naphade, A. L. Gutiérrez, J.-L. Brédas, O. M. Bakr, and O. F. Mohammed, "Modulation of Broadband Emissions in Two-Dimensional 100-Oriented Ruddlesden-Popper Hybrid Perovskites," *ACS Energy Letters* 5 (2020): 2149–2155, https://doi.org/10.1021/acsenergylett.0c01047.

11. Z. Z. Ma, Z. F. Shi, D. W. Yang, et al., "High Color-Rendering Index and Stable White Light-Emitting Diodes by Assembling Two Broadband Emissive Self-Trapped Excitons," *Advanced Materials* 33 (2021): 2001367, https://doi.org/10.1002/adma.202001367.

12. J. Wu, E. Zhou, A. Huang, H. B. Zhang, M. Hu, and G. Z. Qin, "Deep-Potential Enabled Multiscale Simulation of Gallium Nitride Devices on Boron Arsenide Cooling Substrates," *Nature Communications* 15 (2024): 2540, https://doi.org/10.1038/s41467-024-46806-7.

13. J. S. Kang, M. Li, H. Wu, H. Nguyen, T. Aoki, and Y. J. Hu, "Integration of Boron Arsenide Cooling Substrates into Gallium Nitride Devices," *Nature Electronics* 4 (2021): 416–423, https://doi.org/10.1038/s41928-021-00595-9.

14. W. L. Song, P. Wang, L. Cao, et al., "Polymer/Boron Nitride Nanocomposite Materials for Superior Thermal Transport Performance," *Angewandte Chemie, International Edition* 51 (2012): 6498–6501, https://doi.org/10.1002/anie.201201689.

15. J. E. Ryu, S. Park, Y. Park, S. W. Ryu, K. Hwang, and H. W. Jang, "Technological Breakthroughs in Chip Fabrication, Transfer, and Color Conversion for High-Performance Micro-LED Displays," *Advanced Materials* 35 (2023): 2204947, https://doi.org/10.1002/adma.202204947.

16. S. Shin, H. Lee, W. Lee, S. Lee, K. J. Lim, and H. Cho, "High-Efficiency Quantum Dot Permeable Electrode Light-Emitting Triodes for Visible Light Communications and On-Device Data Encryption," *Advanced Materials* 25 (2025): 2503198–2503209, https://doi.org/10.1002/adma.202503189.

17. L. Jin, G. S. Selopal, X. Tong, D. F. Perepichka, Z. M. Wang, and F. Rosei, "Heavy-Metal-Free Colloidal Quantum Dots: Progress and Opportunities in Solar Technologies," *Advanced Materials* 36 (2024): 2402912, https://doi.org/10.1002/adma.202402912.

18. J. R. Li and X. Gong, "Solvent-Induced Self-Assembly Strategy to Synthesize Multicolor Graphene Quantum Dots," *Advanced Functional Materials* 35 (2025): 2504103, https://doi.org/10.1002/adfm.202504103.

19. L. Qian, Y. Zheng, J. Xue, and P. H. Holloway, "Stable and Efficient Quantum-Dot Light-Emitting Diodes Based on Solution-Processed Multilayer Structures," *Nature Photonics* 5 (2011): 543–548, https://doi.org/10.1038/nphoton.2011.171.

20. P. Kumar, P. Devi, R. Jain, et al., "Quantum Dot Activated Indium Gallium Nitride on Silicon as Photoanode for Solar Hydrogen Generation," *Communications Chemistry* 2 (2019): 4, https://doi.org/10.1038/s42004-018-0105-0.

21. H. J. Qiu, J. N. Wu, M. Li, et al., "Oxygen-Doped Colloidal GaN Quantum Dots with Blue Emission," *Materials Today Chemistry* 35 (2024): 101888, https://doi.org/10.1016/j.mtchem.2023.101888.

22. Y. M. Ding, P. He, S. H. Li, et al., "Efficient Full-Color Boron Nitride Quantum Dots for Thermostable Flexible Displays," *ACS Nano* 15 (2021): 14610–14617, https://doi.org/10.1021/acsnano.1c04321.

23. W. B. Wang, Y. X. Wang, K. X. Jin, X. Y. Yang, Y. M. Sui, and B. Zou, "Towards Efficient White-light Emission in Sulfur Dots through Surface Charge Engineering," *Angewandte Chemie, International Edition* 64 (2025): 202415383, https://doi.org/10.1002/anie.202415383.

24. W. T. Li, H. Z. Guo, G. Li, et al., "White Luminescent Single-Crystalline Chlorinated Graphene Quantum Dots," *Nanoscale Horizons* 5 (2020): 928–933, https://doi.org/10.1039/D0NH00053A.

25. S. Y. Lu, L. Z. Sui, Y. Liu, et al., "White Photoluminescent Ti_3C_2 MXene Quantum Dots with Two-Photon Fluorescence," *Advanced Science* 6, no. 9 (2019): 1801470–1801479, https://doi.org/10.1002/advs.201801470.

26. R. Sekiya, Y. Uemura, H. Murakami, and T. Haino, "White-Light-Emitting Edge-Functionalized Graphene Quantum Dots," *Angewandte Chemie, International Edition* 53 (2014): 5619–5623, https://doi.org/10.1002/anie.201311248.

27. T. Yuan, F. L. Yuan, X. H. Li, Y. C. Li, L. Z. Fan, and S. H. Yang, "Fluorescence-Phosphorescence Dual Emissive Carbon Nitride Quantum Dots Show 25% White Emission Efficiency Enabling Single-Component WLEDs," *Chemical Science* 10 (2019): 9801–9806, https://doi.org/10.1039/C9SC03492G.

28. D. Haldar, A. Ghosh, S. Bose, S. Mondal, U. K. Ghorai, and K. K. Saha, "Defect Induced Photoluminescence in MoS_2 Quantum Dots and Effect of

Eu^{3+}/Tb^{3+} Co-Doping Towards Efficient White Light Emission," *Optical Materials* 79 (2018): 12–20, https://doi.org/10.1016/j.optmat.2018.03.012.

29. Z. Liu, L. Tan, P. P. Hou, et al., "One-Pot Synthesis of Single-Component Graphene Quantum Dots for Stable and Bright White Luminescence Films as a Phosphor," *Optical Materials* 127 (2022): 112368, https://doi.org/10.1016/j.optmat.2022.112368.

30. J. Y. Zhu, X. Bai, Y. Zhai, et al., "Carbon Dots with Efficient Solid-State Photoluminescence Towards White Light-Emitting Diodes," *Journal of Materials Chemistry C* 5 (2017): 11416–11420, https://doi.org/10.1039/C7TC04155A.

31. A. Panniello, A. E. D. Mauroa, E. Fanizza, et al., "Luminescent Oil-Soluble Carbon Dots Toward White Light Emission: A Spectroscopic Study," *The Journal of Physical Chemistry C* 122 (2018): 839–849, https://doi.org/10.1021/acs.jpcc.7b09788.

32. T. Y. Zhang, F. F. Zhao, L. Li, et al., "Tricolor White-Light-Emitting Carbon Dots with Multiple-cores@shell Structure for WLED Application," *ACS Applied Materials & Interfaces* 10 (2018): 19796–19805, https://doi.org/10.1021/acsami.8b03529.

33. N. F. Md Noor, M. A. S. Badri, M. M. Salleh, and A. A. Umar, "Synthesis of White Fluorescent Pyrrolic Nitrogen-Doped Graphene Quantum Dots," *Optical Materials* 83 (2018): 306–314, https://doi.org/10.1016/j.optmat.2018.06.040.

34. Y. M. Ding, Q. Chang, F. Xiu, et al., "Zero- and Two-Dimensional Hybrid Carbon Phosphors for High Colorimetric Purity White Light-Emission," *Nanoscale* 10 (2018): 4189–4193, https://doi.org/10.1039/C7NR09631C.

35. B. Bommalingaiah, N. Gaonkar, and R. G. Vaidya, "Effect of Spontaneous Polarization Field on Diffusion Thermopower in AlGaN/GaN Heterostructures," *Chemical Physics Impact* 7 (2023): 100251, https://doi.org/10.1016/j.chphi.2023.100251.

36. W. J. Wang, J. Wu, Y. X. Xing, and Z. H. Wang, "Solvent-Dependent Red Emissive Carbon Dots and Their Applications in Sensing and Solid-State Luminescence," *Sensors and Actuators B Chemical* 360 (2022): 131645–131655, https://doi.org/10.1016/j.snb.2022.131645.

37. S. Khan, A. Gupta, N. C. Verma, and C. K. Nandi, "Time-Resolved Emission Reveals Ensemble of Emissive States as the Origin of Multicolor Fluorescence in Carbon Dots," *Nano Letters* 15 (2015): 8300–8305, https://doi.org/10.1021/acs.nanolett.5b03915.

38. Y. Han, J. Yin, G. Y. Cao, et al., "Exciton Self-Trapping for White Emission in 100-Oriented Two-Dimensional Perovskites Via Halogen Substitution," *ACS Energy Letters* 7 (2022): 453–460, https://doi.org/10.1021/acsenergylett.1c02572.

39. M. L. Liu, Y. H. Xu, Y. Wang, et al., "Boron Nitride Quantum Dots with Solvent-Regulated Blue/Green Photoluminescence and Electrochemiluminescent Behavior for Versatile Applications," *Advanced Optical Materials* 5 (2017): 1600661–1600673, https://doi.org/10.1002/adom.201600661.

40. L. Hidayatova, C. J. Mi, N. G. Akhmedov, et al., "Efficient Mn^{2+} Doping in Non-Stoichiometric Cesium Lead Bromide Perovskite Quantum Dots," *Journal of the American Chemical Society* 147 (2025): 35069–35080, https://doi.org/10.1021/jacs.5c12086.

41. Y. Z. Jiang, C. J. Sun, J. Xu, et al., "Synthesis-on-Substrate of Quantum Dot Solids," *Nature* 612 (2022): 679–684, https://doi.org/10.1038/s41586-022-05486-3.

42. C. Chen, J. M. Wang, D. Liu, et al., "Functionalized Boron Nitride Membranes with Ultrafast Solvent Transport Performance for Molecular Separation," *Nature Communications* 9 (2018): 1902–1910, https://doi.org/10.1038/s41467-018-04294-6.

43. L. Wang, S. J. Zhu, H. Y. Wang, et al., "Common Origin of Green Carbon Dots Luminescence in Carbon Nanodots and Graphene Quantum Dots," *ACS Nano* 8 (2014): 2541–2647, https://doi.org/10.1021/nn500368m.

44. F. L. Yuan, T. Yuan, L. Z. Sui, et al., "Engineering Triangular Carbon Quantum Dots with Unprecedented Narrow Bandwidth Emission for Multicolored LEDs," *Nature Communications* 9 (2018): 2249–2260, https://doi.org/10.1038/s41467-018-04635-5.

45. S. Kaniyankandy, S. Rawalekar, S. Verma, D. K. Palit, and H. N. Ghosh, "Charge Carrier Dynamics in Thiol Capped CdTe Quantum Dots," *Physical Chemistry Chemical Physics* 12 (2010): 4210–4216, https://doi.org/10.1039/b921130f.

46. F. L. Yuan, Y. K. Wang, G. Sharma, et al., "Bright High-Colour-Purity Deep-Blue Carbon Dot Light-Emitting Diodes Via Efficient Edge Amination," *Nature Photonics* 14 (2019): 171–176, https://doi.org/10.1038/s41566-019-0557-5.

47. S. Lee, J. Lee, and S. Jeon, "Aggregation-Induced Emission of Matrix-Free Graphene Quantum Dots via Selective Edge Functionalization of Rotor Molecules," *Science Advances* 9 (2023): ade2585, https://doi.org/10.1126/sciadv.ade2585.

48. R. Bernhardt, M. Manrho, J. Zablocki, et al., "Structural Disorder as the Origin of Optical Properties and Spectral Dynamics in Squaraine Nano-Aggregates," *Journal of the American Chemical Society* 144 (2022): 19372–19381, https://doi.org/10.1021/jacs.2c07064.

49. T. Cao, S. Chen, F. Fang, et al., "Size Effects of 1,2-Ethanedithiol-Treated PbS Quantum Dots on Short-Wave Infrared Photodetector Hole Transport Layers," *The Journal of Physical Chemistry Letters* 16 (2025): 4607–4614, https://doi.org/10.1021/acs.jpclett.5c01032.

50. X. Liu, B. Luo, L. Jin, J. B. Liu, D. Benetti, and F. Rosei, "Ligand-Engineered Cu–Zn–In–Se Quantum Dots for Flexible Laminated Luminescent Solar Concentrators," *Journal of Materials Chemistry A* 14 (2026): 11641–11650, https://doi.org/10.1039/D5TA10030E.

51. S. Thuneibat, H. A. Issa, and A. Ijjeh, "A Simplified Model of Bit Error Rate Calculation," *Computer and Information Science* 9 (2016): 41–46, https://doi.org/10.5539/cis.v9n1p41.

52. Y. Zhao, S. J. Jiao, S. Yang, et al., "High-Performance All-Inorganic Perovskite Tandem Photodetectors with Bi_2TeO_6 Layer Enabled by Enhanced Dual Pyro-Phototronic Effect for Triple-Encryption Imaging Sensing System with Programmable Logic Gate," *Advanced Materials* 37 (2025): 2414649, https://doi.org/10.1002/adma.202414649.

Supporting Information

Additional supporting information can be found online in the Supporting Information section.

Supporting File: adfm75869-sup-0001-SuppMat.docx.